

High Energy Storage Capabilities of $\text{CaCu}_3\text{Ti}_4\text{O}_{12}$ for Paper-Based Zinc-Air Battery

Upasana Bhardwaj

Malaviya National Institute of Technology Jaipur

Aditi Sharma

Malaviya National Institute of Technology Jaipur

Vinay Gupta

Khalifa University of Science and Technology

H.S Kushwaha (✉ himmatsingh.mrc@mnit.ac.in)

Malaviya National Institute of Technology Jaipur

Research Article

Keywords: Zinc-air battery, $\text{CaCu}_3\text{Ti}_4\text{O}_{12}$ (CCTO), Perovskite catalysts, Oxygen Reduction Reaction, Oxygen Evolution Reaction.

Posted Date: December 1st, 2021

DOI: <https://doi.org/10.21203/rs.3.rs-1118935/v1>

License: © ⓘ This work is licensed under a Creative Commons Attribution 4.0 International License.

[Read Full License](#)

Version of Record: A version of this preprint was published at Scientific Reports on March 7th, 2022. See the published version at <https://doi.org/10.1038/s41598-022-07858-1>.

High energy storage capabilities of $\text{CaCu}_3\text{Ti}_4\text{O}_{12}$ for paper-based zinc-air battery

Upasana Bhardwaj^a, Aditi Sharma^a, Vinay Gupta^b H.S Kushwaha^{a*}

^a Materials Research Centre, Malaviya National Institute of Technology Jaipur, Rajasthan, India-302017

^b Department of Physics, Khalifa University of Science and Technology, Abu Dhabi 127788, United Arab Emirates

^{a*}Corresponding author, e-mail: himmatsingh.mrc@mnit.ac.in;

Address: Materials Research Centre, MNITJ, India.

Abstract-

A new perovskite material, $\text{CaCu}_3\text{Ti}_4\text{O}_{12}$ (CCTO), is proposed as an efficacious electrocatalyst for oxygen evolution/reduction reactions for the development of zinc-air batteries (ZAB). Synthesis of this material adopted an effective oxalate route, which led to the purity in the electrocatalyst composition. The CCTO material is a proven potential candidate for energy applications because of its high dielectric permittivity (ϵ) and occupies an improved ORR activity with better onset potential, current density, and stability. The CCTO perovskite was also evaluated for the zinc-air battery as an air electrode, corresponding to the high specific capacitance of 1165 mAh g^{-1} with the greater cyclic efficiency and minimum variations in both charge/discharge processes. The highest power density (P_{max}) measured was 32 mW cm^{-2} . The OCV (Open Circuit Potential) obtained was 1.44 V for the as-developed battery. Also, the CCTO based paper battery shows an excellent performance achieving a specific capacity of $947.79 \text{ mAh g}^{-1}$. The obtained results promise CCTO as a potential and cheap electrocatalyst for application in energy applications.

Keywords: Zinc-air battery; $\text{CaCu}_3\text{Ti}_4\text{O}_{12}$ (CCTO); Perovskite catalysts; Oxygen Reduction Reaction; Oxygen Evolution Reaction.

Highlights:

- The novel aspect of this work is the development of a ZAB using a new perovskite electrocatalyst $\text{CaCu}_3\text{Ti}_4\text{O}_{12}$ (CCTO).
- The electrode preparation employs PVDF to create hydrophobicity and to avoid excessive wetting.
- The CCTO ZAB delivers impressive specific capacitance and excellent stability.

1 Introduction-

In the recent energy scenario, the energy storage and harvesting are pretty dependent on oxygen electrochemistry via metal-air batteries and fuel cells¹. Zinc-air batteries have attained much attention in developing portable electronic devices, electric vehicles, and grid storage²⁻⁵. An excellent energy density up to 1353 W h kg^{-1} zinc-air batteries perform five times better than lithium-ion batteries^{6,7}. The abundance, low cost, eco-friendliness, less toxicity, high stability in alkaline and aqueous medium, and no requirement of manufacturing environment are also the advantages of the zinc-air batteries, which makes them a promising option for clean energy storage^{8,9,10}. The intrinsic lethargic process of the oxygen reduction reaction (ORR) and oxygen evolution reaction (OER) on the air electrode results in a vast over potential, impoverished reversibility, constrained energy efficiency, and low output power density technical barriers the practical application of ZABs¹¹⁻¹³. The ORR-OER reactions are the primary electro-chemical processes that regulate various electrochemistry-based applications like energy conversion and storage devices¹⁴. Until recently, platinum (Pt) and platinum alloys have been identified as the most effective ORR catalysts, although they exhibit weak OER performance.

On the other hand, the most excellent catalyst for OER is Iridium (IrO_2) or Ruthenium oxide (RuO_2), but it shows weak ORR activity¹⁵. Worryingly, the high price, paucity, and poor stability of RuO_2 , Pt, and IrO_2 -based oxygen materials have impeded their widespread use. As a result, much effort has been expended in the quest for low-cost metal-free noble bi-functional catalysts for OER and ORR in alkaline medium, like, metal oxides, chalcogenides, double-layered hydroxides, spinels, and perovskites^{14,16}.

Perovskites are materials with high electro-catalytic activities and the capabilities to tune up their structural stability and composition flexibility^{1,3}. They are also relatively cheap with a high specific activity. They have the formula of ABO_3 where A site occupies rare/alkaline earth metal cations (12 fold coordination), and B site occupies transition metal cations (6 fold coordination)^{17,18}. The perovskites are also widely useful in oxygen transport membrane, water splitting, and solid oxide fuel cells (SOFCs) due to their excellent electronic/ionic conductivity and defects^{1,3,12}.

Suntivich et al. stated that using B-site transition metals with, e.g., occupancy near unity can improve the catalytic kinetics for OER. In the oxygen-transition metal complex at the B-site, the covalency between the 3d orbital of metal and the 2p orbitals of oxygen regulates the catalysis activity of ABO_3 perovskite by enhancing charge movement in the rate-determining stages (RDS). However, this is sometimes rejected as it is not mandatory for a perovskite catalyst to show ORR/OER activities. Also, the oxygen vacancies play a vital role in the determination of ORR/OER in perovskites. While in electrocatalysis, oxygen vacancies in perovskite catalyst (ABO_3) can act as acceptors or donors, increasing charge transport between catalyst surface and absorbed species¹⁹⁻²¹.

An air electrode is a crucial component of a battery, i.e., a poorly defined cathode will have low energy efficiency, increased overpotential, and poor cyclability. Therefore, the effectiveness of an air-cathode is evaluated by a variety of variables, including inner porosity, effectual surface area,

porous mass activity, surface wettability, and agglomeration size. The zinc-air batteries usually suffer wettability issues with the gas diffusion electrodes, i.e., the pores in the porous electrode get blocked by the electrolyte, reducing the rate of oxygen diffusion at the surface of the electrode, hence, reducing the efficient performance of the battery. The typical aqueous Zn-air cells are metal-air batteries that need balanced hydrophilicity and hydrophobicity in the air cathode with a three-phase boundary. To prevent electrolyte overflow in the electrode pores and facilitate O₂ diffusion at the activation sites, hydrophobic additives such as PVDF, PTFE were added to partly wet the electrode²². The majority of the electrocatalyst nanoparticles (like 80% Pt) were found in the tiny primary holes that serve as reaction volumes. In contrast, the majority of the Polytetrafluoroethylene is located in the bigger secondary pores that act as pre-eminent gas routes²².

CaCu₃Ti₄O₁₂ is a cubic (AA'BO₃) double-perovskite bi-functional electrocatalyst with an AA'BO₃ formulation. The Ca²⁺ is located on the A site with Cu²⁺ at the A' space, and the Ti⁴⁺ is structured on site B. To create JahnTeller distortion in Cu²⁺, the distorted octahedral TiO₆ produces a square planar structure^{1,23,24}. Without doping, the prolonged structure incorporates open-shell Cu²⁺ and Ti⁴⁺ within CCTO, and both cations fill particular positions within the crystal structure. CCTO perovskite is also a propitious electrocatalyst due to its great dielectric permittivity (ε) up to 300 000, making it suitably efficient for energy applications^{25,26}. Also, each oxygen atom in CCTO forms a strong covalent bond with an ion of A'-Cu²⁺ and double ions of B-Ti⁴⁺. As a result, the movement of charge between A'-Cu and B-Ti ions is crucial in electro-catalytic activity²⁷⁻²⁹.

Therefore, the novelty in this work is the application of CaCu₃Ti₄O₁₂ (CCTO) for the first-ever time in the field of batteries employing paper as an electrolyte substrate. In this research report, we extensively synthesize and investigate the bi-functional properties of the perovskite material for electrochemical characterization, i.e., ORR-OER with its application efficiency in ZAB.

2 Results and discussion-

2.1 Physical characterization:

The CCTO powder was prepared employing an oxalate precursor route. The material obtained was earth brown in color. XRD characterization was conducted to obtain the crystal structure and phase composition of the material, as shown in figure 1. The XRD patterns were obtained on the as-prepared CCTO catalyst shown in the figure.1(a) perfectly matching the ICDD data no. 01-075-1149 displayed in figure.1(b). The results state the single-phase nature of the CCTO sample as there are no residual peaks of CuO and TiO₂ using this synthesis route. The crystallite size for CCTO was calculated to be 26 nm employing the Scherrer formula:

$$D = \frac{K\lambda}{\beta \cos\theta} \quad (1)$$

Where,

D is the size of crystallite; K is 0.9 (Scherrer constant); λ is 0.1546 nm; β is FWHM and Θ is the position of the peak in the formula.

XPS was also done to recognize the chemical composition, valence ions, and the species oxygenated. Figure S.1 reveals the entire XPS spectra of CCTO with peaks of Ca 2*p*, Cu 2*p*_{3/2}, Cu 2*p*_{1/2}, Ti 2*p*_{3/2}, and O 1*s* at respective binding energies. Figure.2 (a) demonstrates the Ca 2*p* spectra of CCTO are best fitted with Ca 2*p*_{1/2} and Ca 2*p*_{3/2}, two spin-orbit doublets obtaining peaks at early binding energies. The peak of Ca 2*p*_{3/2} de-convolutes and splits into peaks at 346.76 eV and 347.42 eV, whereas Ca 2*p*_{1/2} was found at 350.62 eV. Figure.2 (b) shows the Cu 2*p* spectra of CCTO acquiring Cu 2*p*_{3/2} de-convoluted peaks at 932.19 eV, 932.53 eV, and Cu 2*p*_{1/2} at 952.14 eV. The Figure.2 (c) shows the Ti 2*p* region where Ti 2*p*_{3/2} acquires peak at 458.38 eV and Ti 2*p*_{1/2} at 464.01 eV. The O 1*s* spectra of CCTO are shown in Figure.2 (d). Based on lattice oxygen species (O²⁻), highly oxidative oxygen species (O₂⁻/O⁻), molecular water adsorbed (H₂O), and surface

adsorbed oxygen or hydroxyl groups, the O 1s spectra of CCTO were de-convoluted into peaks at 530.7 and 531.27 eV. (OH^- or O_2). The O_2 vacancies on the surface, as shown by ($\text{O}_2^{2-}/\text{O}^-$), are advantageous for ORR catalysis. Also, the oxygen vacancies can be binded with the absorbed oxygen, thus, increasing ORR activity²⁴. An EDX analysis also confirms the formation of $\text{CaCu}_3\text{Ti}_4\text{O}_{12}$ perovskite catalyst by focussing on various areas during an EDX measurement to obtain the respective peaks, as are depicted in Figure.S2. In an EDX spectrum, the CCTO can be seen synthesized, with the quantities of Ca, Cu, Ti, and O measured in atomic percent to be 1.35, 10.20, 7.87, and 1.71%, respectively. Table S1 shows the specifics of EDX spectra for the $\text{CaCu}_3\text{Ti}_4\text{O}_{12}$ sample. Scanning electron micrographs were also obtained to investigate the structure of the Ni foam loaded with the catalyst and to analyze the distribution of the material ink on the cathode, as shown in Figure.3 (a & b). The EDS (Energy Dispersive X-ray Spectroscopy) elemental map displays the CCTO compound was well dispersed on the surface of the Nickel foam at the tens-of-micrometer scale producing the best catalytic results. Figure.3 (c-h) shows the elemental distribution of Ca, Ni, Cu, O, Ti and C. The elements are seen well dispersed on the electrode surface. The CCTO catalyst was quantified with Cu and Ti in abundance, which acts as prime sites for the electro-catalytic activity for the sluggish oxygen reactions. Also, the O_2 can be seen in a considerate quantity leading to enhanced performance. Figure.S3 (a & b) shows the N_2 desorption/adsorption isotherm and multi-point graph of CCTO to check the porosity and surface area of the perovskite material. The CCTO material exhibits a surface area of 2.312 m^2/g with a pore radius of 1.09724 nm.

2.2 Electrochemical characterization:

To assess the electro-chemical behavior, the OER and ORR measurements were taken on the Nova instrument using a three electrodes system comprising of glassy carbon rotating disk electrode (5 mm; RDE) as working electrode, Ag/AgCl and Pt wire as reference and counter electrodes in KOH solution (0.1 M). Before evaluation, the electrolyte was infused with N_2 gas followed by O_2

gas for almost 30 minutes. LSV (Linear sweep voltammetry) was used to detect the oxygen reduction behavior of the perovskite material in the voltage range of 1.5 to -0.5 V (vs. RHE) at the scan rate of 20 mV s⁻¹ at various rotation speeds from 0-2400 rpm. Previous research has shown that the transition metals and the oxygen species act as an active site for oxygen reactions. They have the ability to improve the structure and thus increase conductivity³. The best ORR catalysts have distinct surface planes and high surface water content. The ORR trend can be validly indicated by the E_{1/2}, as it is commonly used to analyze the ORR catalytic activity of the electrocatalysts. Therefore Figure.4 (a) shows the ORR trend with the E_{onset} of 1.10 V and the half-wave potential (E_{1/2}) of 0.70 V.

The current density of the CCTO sample was seen to be steadily increasing with the rotation speeds, which shows enhancement in the diffusion regulated procedure. In Figure.4 (b) K-L (Koutecky – Levich) graph was obtained using an equation shown to demonstrate the ORR pathway

$$1/I = 1/I_k + 1/I_{lev} \quad (2)$$

Where the current-density is given by I, I_{lev} is Levich current-density, and I_k is Kinetic current density, respectively.

$$I_k = nFAkO_2 CO_2 \gamma_{catalyst} \quad (3)$$

$$I_{lev} = 0.62nFAC_{O_2} D_{O_2}^{2/3} \nu^{-1/6} \omega^{1/2} \quad (4)$$

Where, $\nu = 1 \times 10^{-6} \text{ m}^2 \text{ s}^{-1}$ in KOH solution (0.1 M), ω - angular frequency of rotation (rad s⁻¹), D_{O₂} - O₂ diffusion coefficient ($1.87 \times 10^{-9} \text{ m}^2 \text{ s}^{-1}$ in 0.1 M KOH solution), $\gamma_{catalyst}$ - surface concentration of the catalyst (49.8 $\mu\text{g cm}^{-2}$), C_{O₂} - concentration of oxygen dissolved (1.21 mol m⁻³ in KOH 0.1 M solution), k_{O₂} - rate constant for ORR (m s⁻¹), F - Faradaic constant (96 485 C mol⁻¹) and n - electrons transfer during ORR, A – the area of an electrode.

The I_{lev} is directly proportional to the square root of the rate of rotation of an electrode. In the limited diffusion region, a graph of (J⁻¹ (mA cm⁻²)⁻¹ vs. 1/ ω (K-L plot) was drawn. The linear

nature of the graph exhibited 1st order kinetics during ORR, and the number of transferred electron was calculated to be 4. According to this assessment, chasing the 4 electron pathway, CCTO can be effective at reducing O₂.

To further analyze the perovskite material for oxygen evolution (OER), Linear Sweep Voltammetry (LSV) was conducted in the voltage range of 1.02 to 2.5 V at a scan rate of 10 mV s⁻¹ as shown in Figure.5 (a). With the onset potential (E_{onset}) set to 1.48 V, the graph depicts the sample's oxygen evolution reaction capability (vs. RHE). In the OER LSV curves, the overpotential (η) yielding a current density of 1 mA cm⁻² is given as E_{j=1}. The E_{j=1} value of CCTO came to be 1.61 V. The Tafel slope at the onset potential was calculated to observe the rate of reaction. The Tafel slope was obtained using this equation as shown in Figure.5 (b):

$$\eta = b \log J \quad (5)$$

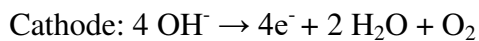
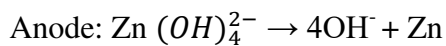
Using this equation, the Tafel slope was determined to be 80 mV dec⁻¹. The following equation determines the potential difference (ΔE) at the oxygen electrode:

$$\Delta E = E_{j=1}OER - E_{1/2}ORR \quad (6)$$

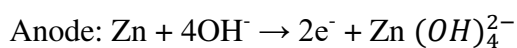
The lower ΔE results in good capability in terms of OER-ORR. As a result, ΔE = 0.9 V for CCTO at the voltage complementing to 1 mA cm⁻² for OER and E_{1/2} in ORR at 2400 rpm, i.e., 1.61 – 0.7 V, demonstrates its bi-functionality.

2.3 Zinc-air battery performance -

Charging-



Discharging-



The metal-air battery's (MAB) behavior is accredited to the redox activity of its transition metals and the interaction of orbitals. The ZAB was conceived & built to investigate and improve the efficiency, capacity, and durability of the $\text{CaCu}_3\text{Ti}_4\text{O}_{12}$ catalyst in conjunction with the electrolyte. To assess the performance of the as-prepared catalyst in energy storage application, Two different batteries were developed: (i) a primary aqueous $\text{CaCu}_3\text{Ti}_4\text{O}_{12}$ battery, (ii) a rechargeable $\text{CaCu}_3\text{Ti}_4\text{O}_{12}$ based paper ZAB.

The aqueous zinc-air battery (ZAB) setup was developed and evaluated in 6 M KOH + 0.2 M $\text{Zn}(\text{Ac})_2$ electrolyte for the energy applications, The charge/discharge curve for rechargeable ZAB is demonstrated in Figure.6 (a). The highest power density (P_{max}) was measured to be 32 mW cm^{-2} . The aqueous ZAB, when being discharged galvanostatically at 5 mA cm^{-2} , commits a constant discharge potential $\sim 0.12 \text{ V}$, as shown in Figure.6 (b). The calculated specific capacity of an aqueous CCTO ZAB at the current density of 5 mA cm^{-2} came out to be as good as 1165 mAh g^{-1} normalized to the consumed mass of zinc with the discharge rate to be 0.038 Ah . The chronopotentiometry charge/discharge test was used to determine the durability and cyclic efficiency of the battery, as shown in Figure.6 (c). The charge/discharge profile shows the stable performance of the cell with lower overpotential during the entire test. The charge/discharge potentials of the aqueous ZAB with the cell cycle were approximately 1.4 to 2.2 V at the current scan of 10 mA , respectively, corresponding to the charge/discharge overpotential (η) of 0.8 V . The corresponding round trip efficiency was determined by the formula: $\frac{E_{\text{Discharge}}}{E_{\text{Charge}}}$ Where $E_{\text{Discharge}}$ and E_{Charge} are the final potentials of the charge/discharge profiles for the respective cycles. Therefore, the round-trip efficiency was determined to be 63% for the aqueous battery. Furthermore, the straight potential graphs in Figure.6 (d) demonstrate CCTO to be an efficient bifunctional

electrocatalyst for the paper-based zinc-air battery due to its greater cyclic efficiency and minimum variations in both charge/discharge processes.

The flexible and eco-friendly ZABs have attracted significant research attention due to the advancement in energy storage devices. In this study, a flexible and eco-friendly solid-state rechargeable ZAB was developed by loading $\text{CaCu}_3\text{Ti}_4\text{O}_{12}$ on nickel foam (cathode) and zinc foil (anode) with the 6M KOH + 0.2M $\text{Zn}(\text{Ac})_2$ electrolyte soaked in Whatman filter paper. Paper's porous morphology allows the electrolyte to diffuse efficiently, allowing it to be used effectively. The galvanodynamic LSV technique (Current Density vs. Voltage) was employed to elucidate the charge/discharge polarisation curves for chargeable zinc-air batteries. As shown in Figure.7 (a), galvanodynamic discharge-charge (current density vs. voltage) polarisation plots were taken at varied current values, at the current density ranging from 0-25 mA cm^{-2} . Figure.7 (b) depicts the maximum power density from the current density vs. power density polarization curve. The power density indicates the current storing capabilities of a cell, which is 5.5 mW cm^{-2} at 11.45 mA cm^{-2} for the KOH-filter paper battery. It was recognized that the power density increases with increasing scan rates from 10 mA/s to 600 mA/s. To determine the discharge capabilities and storing capacity of the paper-based ZAB, a discharge profile was obtained. Figure.7 (c) reveals the discharge curve (Capacity (mAh g^{-1}) vs. Potential (V) at 5 mA cm^{-2} . In ambient air, the material was determined to remain stable for good hours. This consequence in a firm discharge potential of $\sim 1.11 \text{ V}$. The specific capacity of the paper-based ZAB was calculated to be $947.79 \text{ mAh g}^{-1}$. For evaluating the cyclic efficiency and durability of the battery, the chrono-potentiometric charge/discharge plot for CCTO at a current density of 10 mA cm^{-2} is shown in Figure.7 (d). Even after 3.5 hours of continuous use, the filter paper battery was determined to be stable within a voltage range of 1.5-2.0 V. Gradually, as the potential is obtained at 2.0 V with a constant voltage gap recommending good stability. As demonstrated in insight, the cell voltage over-potential remain constant, i.e., 0.50 V, throughout the run of 3.5 hours, indicating good stability

characteristics, and the corresponding round trip efficiency was determined to be 75% for the filter paper battery thus, proving itself an efficient zinc-air battery. A comparison plot is shown in Figure.8 (a), displaying the high capacity of CCTO catalyst amongst other catalysts tested. The OCV (open circuit voltage) of the produced ZAB's was also determined to be 1.44 V, as illustrated in the figure.8 (b).

3 Conclusions-

In summary, we developed a $\text{CaCu}_3\text{Ti}_4\text{O}_{12}$ (CCTO) based ZAB using oxalate-route, showing enhancement in OER, ORR activity, and battery performance. The difference in the potential (ΔE) of CCTO was determined to be 0.9 V, indicating its excellent activity in ZAB. The proposed ZAB was tested under an alkaline system using aqueous and filter paper soaked electrolyte (6 M KOH + 0.2 M $\text{Zn}(\text{Ac})_2$). The zinc-air cell demonstrated remarkable cycling stability for a good time through discharge-charge cycles with an OCV of 1.44 V. The specific capacity achieved by the paper battery was 947.79 mAh g^{-1} . Thus, CCTO may be utilized as an efficient electrocatalyst for rechargeable zinc-air batteries.

4 Methods-

4.1 $\text{CaCu}_3\text{Ti}_4\text{O}_{12}$ synthesis

The $\text{CaCu}_3\text{Ti}_4\text{O}_{12}$ was prepared using an oxalate precursor route^{1,24}. In an ideal preparation, the titania gel was created from aqueous TiOCl_2 (0.05M) by pouring NH_4OH (aq) (at 25°C) until the pH reached 8.0 and then washing off the NH_4Cl using a filter. Powdered titania gel (0.4 moles) $\text{TiO}_2 \cdot x\text{H}_2\text{O}$ (where $92 < x < 118$) was thoroughly mixed to this titania gel without the addition of water. Calcium carbonate was added to the clear solution and stirred. There was no precipitate formation in the solution. After cooling to 10°C, cupric chloride ($\text{CuCl}_2 \cdot 2\text{H}_2\text{O}$) mixed in acetone & water in the ratio of 80:20 was further added and mixed steadily. The dense precipitate was

washed and obtained with acetone several times to remove the chloride and was dried in the air. The residue so formed was heated isothermally above 680°C to yield a CaCu₃Ti₄O₁₂ ceramic catalyst. The powder was carefully ball milled for 2 hours and further calcined for 4 hours at 1130 °C in the air.

4.2 Material characterization-

To investigate the crystal purity and structure of the prepared CCTO material, diffraction tests were performed with an X'pert diffractometer in a wide range of 2θ ($5^\circ \leq 2\theta \leq 85^\circ$) with the step size of 0.0170 using Cu K α_1 radiation ($\lambda = 0.154056$ nm) to evaluate the phase constitutes of the specimens. The X-ray Photo-electron Spectroscopy (XPS) characterization was performed on the Oxford Instruments (ESCA+ model) Omicron Nanotechnology X-ray Photo-electron Spectroscopy system comprising a chamber with ultra-high vacuum connected to a 124 mm hemispherical electron analyzer and 1486.7 eV energy monochromatic source Al-K α radiation. Further to obtain the composition and microstructure of the sintered pellets, FEI-Technai SEM-Sirion (equipped with Energy-Dispersive X-ray spectroscopy (EDX)) SEM (Scanning Electron Microscope) was used. To observe the specific surface area of the perovskite material, Brunauer-Emmett-Teller (BET) study was directed to get the nitrogen sorption isotherms using quantachrome Instruments Nova Touch Lx2, USA.

4.3 Electrochemical characterization-

ORR-OER measurements were performed on a Metrohm Autolab (Electrochemical Workstation) in 0.1 M KOH electrolyte with a three-electrode system. A glassy carbon rotating disk electrode (RDE) with a diameter of 5 mm was taken as a working electrode, the reference electrode was Ag/AgCl, and the counter electrode was platinum wire in KOH electrolyte.

Preparation of slurry for the working electrode-

5 mg CCTO catalyst was mixed with 10 mg of Vulcan carbon XC-72 in mortar-pestle and further dispersed in 2.5 mL Isopropyl alcohol (IPA), and 2.5 mL Distilled water (D.I) to prepare the ink for the cathode. In addition, 300 μL of Nafion solution (5 wt% (w/w)) was added. After an hour of ultra-sonication, 20 μL with the loading mass of $102 \mu\text{g cm}^{-2}$ of the slurry was drop cast over the glassy carbon electrode (RDE) for the electro-chemical characterization.

4.4 Development of Zinc-air cell:

A homemade solid-state paper-based zinc-air cell was fabricated using the CCTO perovskite catalyst. The catalyst was loaded onto a nickel foam as cathode, a filter paper saturated in 6 M KOH + 0.2 M Zn(Ac)₂ as an electrolyte, and a zinc foil as an anode. The cathode was developed by loading a slurry of Carbon black and PVDF in the ratio of 30:70 wt% dispersed in 1 ml of ethanol. The slurry completely coats the outer side of the Ni-foam, creating gas diffusion sites. The electrode is then hot pressed for 15 mins at 350°C. Whereas the slurry for the inner side was prepared by mixing the 35 mg of active perovskite material and 35 mg of carbon black powder in 25 μL of the binder (Nafion solution: 5 wt%) was dispersed 1 ml of IPA using ultra-sonication until a homogenous solution is obtained. 1 ml (loading mass = 0.033 g cm^{-2}) of the slurry was coated on nickel foam (2 cm^2) which was further pressed at 150°C for ten mins³⁰.

To improve the performance of the ZAB, the battery components were assembled using a requisite battery cell under proper pressure. The cell consists of two Teflon sheets with 5 mm thickness containing flexibility in size with the help of four nuts and bolts at each corner. The lower sheet includes a platform where the entire battery component rests, i.e., the nickel foam (cathode), the paper-soaked electrolyte, and the zinc foil (anode). For the transport of oxygen, there is a provision of an air-breathing window on the upper Teflon sheet with the size 1.5 cm^2 . As the current collector, copper tapes were pasted to both electrodes, constituting the assembly ultimately.

References-

1. Kushwaha, H. S., Halder, A., Thomas, P. & Vaish, R. CaCu₃Ti₄O₁₂: A Bifunctional Perovskite Electrocatalyst for Oxygen Evolution and Reduction Reaction in Alkaline Medium. *Electrochim. Acta* **252**, 532–540 (2017).
2. Li, Y. *et al.* Advanced zinc-air batteries based on high-performance hybrid electrocatalysts. *Nat. Commun.* **4**, 1805–1807 (2013).
3. Bhardwaj, U., Sharma, A., Mathur, A., Halder, A. & Kushwaha, H. S. Novel guar-gum electrolyte to aggrandize the performance of LaMnO₃ perovskite-based zinc-air batteries. *Electrochem. Sci. Adv.* 1–15 (2021) doi:10.1002/elsa.202100056.
4. Liu, J. *et al.* CoOx/CoNy nanoparticles encapsulated carbon-nitride nanosheets as an efficiently trifunctional electrocatalyst for overall water splitting and Zn-air battery. *Appl. Catal. B Environ.* **279**, 119407 (2020).
5. Ma, Z. *et al.* Novel flower-like nickel sulfide as an efficient electrocatalyst for non-aqueous lithium-air batteries. *Sci. Rep.* **5**, 1–9 (2015).
6. Lee, H. *et al.* Advanced Electrochemical Properties of PrBa_{0.5}Sr_{0.5}Co_{1.9}Ni_{0.1}O_{5+δ} as a Bifunctional Catalyst for Rechargeable Zinc-Air Batteries. *ChemElectroChem* **6**, 3154–3159 (2019).
7. Hosseini, S. *et al.* The Influence of Dimethyl Sulfoxide as Electrolyte Additive on Anodic Dissolution of Alkaline Zinc-Air Flow Battery. *Sci. Rep.* **9**, 1–12 (2019).
8. Wang, Y. *et al.* Continuous fabrication of a MnS/Co nanofibrous air electrode for wide integration of rechargeable zinc-air batteries. *Nanoscale* **9**, 15865–15872 (2017).
9. Wang, H. F. *et al.* Defect-rich carbon fiber electrocatalysts with porous graphene skin for

- flexible solid-state zinc–air batteries. *Energy Storage Mater.* **15**, 124–130 (2018).
10. Xu, N. *et al.* Self-Assembly formation of Bi-functional Co₃O₄/MnO₂-CNTs hybrid catalysts for achieving both high energy/power density and cyclic ability of rechargeable zinc-Air battery. *Sci. Rep.* **6**, 1–10 (2016).
 11. Jung, K. N. *et al.* One-dimensional manganese-cobalt oxide nanofibres as bi-functional cathode catalysts for rechargeable metal-air batteries. *Sci. Rep.* **5**, 1–10 (2015).
 12. Miao, H. *et al.* A-site deficient/excessive effects of LaMnO₃ perovskite as bifunctional oxygen catalyst for zinc-air batteries. *Electrochim. Acta* **333**, 135566 (2020).
 13. Fu, J. *et al.* Flexible High-Energy Polymer-Electrolyte-Based Rechargeable Zinc-Air Batteries. *Adv. Mater.* **27**, 5617–5622 (2015).
 14. Deng, Z. *et al.* NiCo-doped C-N nano-composites for cathodic catalysts of Zn-air batteries in neutral media. *Electrochim. Acta* **279**, 1–9 (2018).
 15. Park, H. S. *et al.* Bifunctional hydrous RuO₂ nanocluster electrocatalyst embedded in carbon matrix for efficient and durable operation of rechargeable zinc-air batteries. *Sci. Rep.* **7**, 1–9 (2017).
 16. Prabu, M., Ramakrishnan, P., Ganesan, P., Manthiram, A. & Shanmugam, S. LaTi_{0.65}Fe_{0.35}O_{3-δ} nanoparticle-decorated nitrogen-doped carbon nanorods as an advanced hierarchical air electrode for rechargeable metal-air batteries. *Nano Energy* **15**, 92–103 (2015).
 17. Bu, Y. *et al.* A Highly Efficient and Robust Cation Ordered Perovskite Oxides as a Bi-Functional Catalyst for Rechargeable Zinc-Air Batteries. (2017)
doi:10.1021/acsnano.7b06595.

18. Wang, Q. *et al.* $\text{La}_{0.8}\text{Sr}_{0.2}\text{Co}_{1-x}\text{Mn}_x\text{O}_3$ perovskites as efficient bi-functional cathode catalysts for rechargeable zinc-air batteries. *Electrochimica Acta* vol. 254 (Elsevier Ltd, 2017).
19. Mueller, D. N., MacHala, M. L., Bluhm, H. & Chueh, W. C. Redox activity of surface oxygen anions in oxygen-deficient perovskite oxides during electrochemical reactions. *Nat. Commun.* **6**, (2015).
20. Chen, C. F. *et al.* Oxygen-deficient BaTiO_{3-x} perovskite as an efficient bifunctional oxygen electrocatalyst. *Nano Energy* **13**, 423–432 (2015).
21. Bian, J., Li, Z., Li, N. & Sun, C. Oxygen Deficient $\text{LaMn}_{0.75}\text{Co}_{0.25}\text{O}_3$ Nanofibers as an Efficient Electrocatalyst for Oxygen Evolution Reaction and Zinc-Air Batteries. *Inorg. Chem.* **58**, 8208–8214 (2019).
22. Cai, X., Lai, L., Lin, J. & Shen, Z. Recent advances in air electrodes for Zn-air batteries: Electrocatalysis and structural design. *Mater. Horizons* **4**, 945–976 (2017).
23. Clark, J. H. *et al.* Visible Light Photo-oxidation of Model Pollutants Using $\text{CaCu}_3\text{Ti}_4\text{O}_{12}$: An Experimental and Theoretical Study of Optical Properties, Electronic Structure, and Selectivity. *J. Am. Chem. Soc.* **133**, 1016–1032 (2011).
24. Kushwaha, H. S. *et al.* Efficient Solar Energy Conversion Using $\text{CaCu}_3\text{Ti}_4\text{O}_{12}$ Photoanode for Photocatalysis and Photoelectrocatalysis. *Sci. Rep.* **6**, 1–10 (2016).
25. Zang, G., Zhang, J., Zheng, P., Wang, J. & Wang, C. Grain boundary effect on the dielectric properties of $\text{CaCu}_3\text{Ti}_4\text{O}_{12}$ ceramics. *J. Phys. D. Appl. Phys.* **38**, 1824–1827 (2005).
26. Fang, T. T. & Liu, C. P. Evidence of the internal domains for inducing the anomalously

- high dielectric constant of $\text{CaCu}_3\text{Ti}_4\text{O}_{12}$. *Chem. Mater.* **17**, 5167–5171 (2005).
27. Matos, M. & Walmsley, L. Cation-oxygen interaction and oxygen stability in $\text{CaCu}_3\text{Ti}_4\text{O}_{12}$ and $\text{CdCu}_3\text{Ti}_4\text{O}_{12}$ lattices. *J. Phys. Condens. Matter* **18**, 1793–1803 (2006).
 28. Mizumaki, M., Saito, T., Shiraki, H. & Shimakawa, Y. Orbital Hybridization and Magnetic Coupling of the A-Site Cu Spins in $\text{CaCu}_3\text{B}_4\text{O}_{12}$ (B = Ti, Ge, and Sn) Perovskites. *Inorg. Chem.* **48**, 3499–3501 (2009).
 29. Кадырова, Н. И., Мельникова, Н. В., Устинова, И. С. & Зайнулин, Ю. Г. Влияние высоких давлений и температур на структуру и свойства $\text{CaCu}_3\text{Ti}_4\text{O}_{12}$. *Неорганические Материалы* **52**, 1122–1125 (2016).
 30. Abbasi, A. *et al.* Discharge profile of a zinc-air flow battery at various electrolyte flow rates and discharge currents. *Sci. Data* **7**, 1–8 (2020).

ACKNOWLEDGEMENTS-

The authors are grateful to the WTI and DST for providing funding under the WTI project and the DST-Inspire faculty scheme.

List of Figures-

- Figure 1:** (a) XRD patterns of (i) as prepared $\text{CaCu}_3\text{Ti}_4\text{O}_{12}$ (CCTO) nano-powder, and (b) ICDD data file card no. 01-075-1149 for CCTO.
- Figure 2:** (a,b,c,d) XPS analysis of the CCTO catalyst.
- Figure 3:** EDS mapping and distribution of the as-prepared $\text{CaCu}_3\text{Ti}_4\text{O}_{12}$ (CCTO) slurry on the electrode: (a) FESEM image of the CCTO coated Ni Foam, (b) The distribution of the CCTO catalyst on the electrode, (c) Cu element (Red), (d) Ni element (Green), (e) Ca element (Pink), (f) O element (Cyan), (g) Ti element (Blue), (h) Carbon element (Yellow).
- Figure 4:** ORR electro-chemical analysis in 0.1M KOH solution, O_2 purged (a) RDE graphs of CCTO at different rotations in the potential range of 1.5 to - 0.5V; (b) Koutecky – Levich graph of the material at various potentials (V).
- Figure 5:** Electro-chemical investigation of OER in 1M KOH solution (N_2 saturated) (a) LSV graphs of CCTO at different rotations between the potentials of 0.0 – 2.4V.
- Figure 6:** Performance of fabricated aqueous zinc-air battery. (a) Charge – Discharge curve with Power density of CCTO; (b) Discharge profile of CCTO at 5 mA cm^{-2} for continuous 30 hours. (c) Charge/discharge (Chronopotentiometric) curve for CCTO at 20 mA cm^{-2} with the potential range of 1.4-2.2 V for an hour (insight: displays charge/discharge polarization (Time vs. Potential) with extended cycles); (d) shows Voltage vs. Number of cycles.
- Figure 7:** Performance of fabricated solid-state ZAB. (a) Charge/Discharge of the cell at various scan rates; (b) CCTO power density; (c) CCTO discharge profile (Capacity vs. Potential) at 5 mA cm^{-2} ; (d) Chronopotentiometric charge/discharge cycles for CCTO at

20 mA with the potential range of 1.5-2.0 V, (insight: shows charge/discharge potential cycles).

- 8. Figure 8:** (a) Battery Potential vs. Cycle Number plot for filter paper battery; (b) Comparison of various zinc-air batteries with CCTO; (c) shows the potential of designed solid-state zinc-air cell giving the OCV of 1.44 V.

Figures

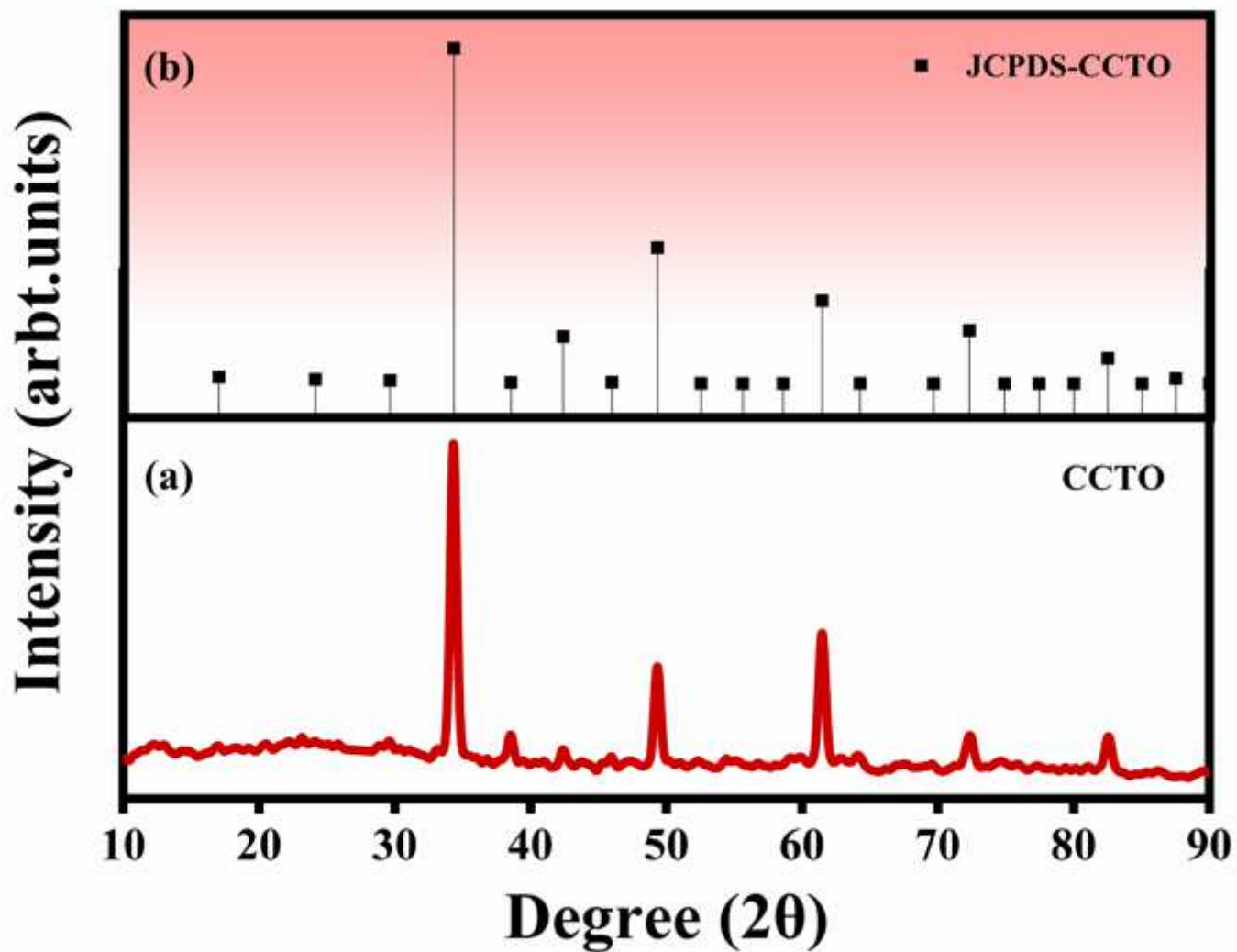


Figure 1

(a) XRD patterns of (i) as prepared $\text{CaCu}_3\text{Ti}_4\text{O}_{12}$ (CCTO) nano-powder, and (b) ICDD data file card no. 01-075-1149 for CCTO.

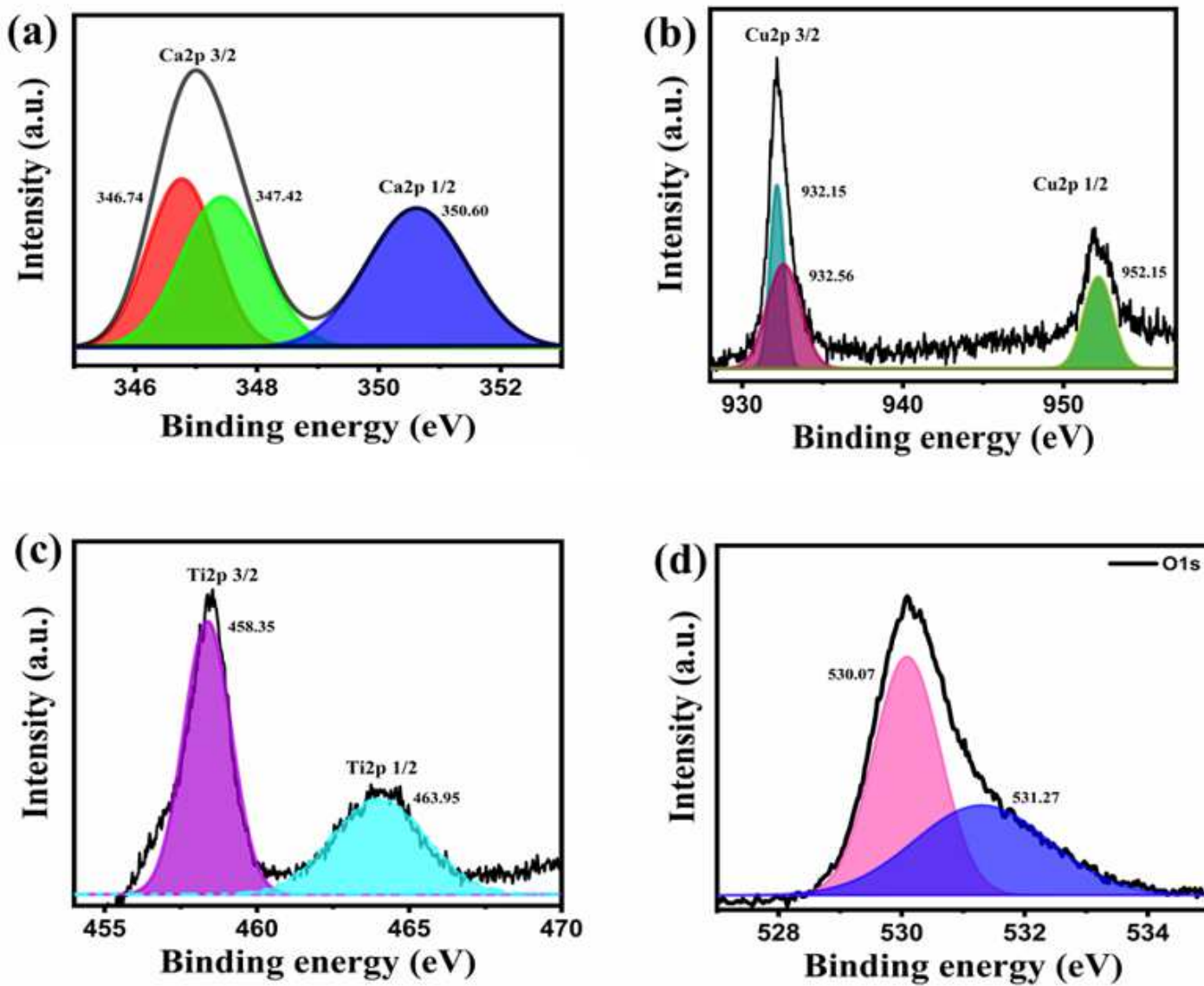


Figure 2

(a,b,c,d) XPS analysis of the CCTO catalyst.

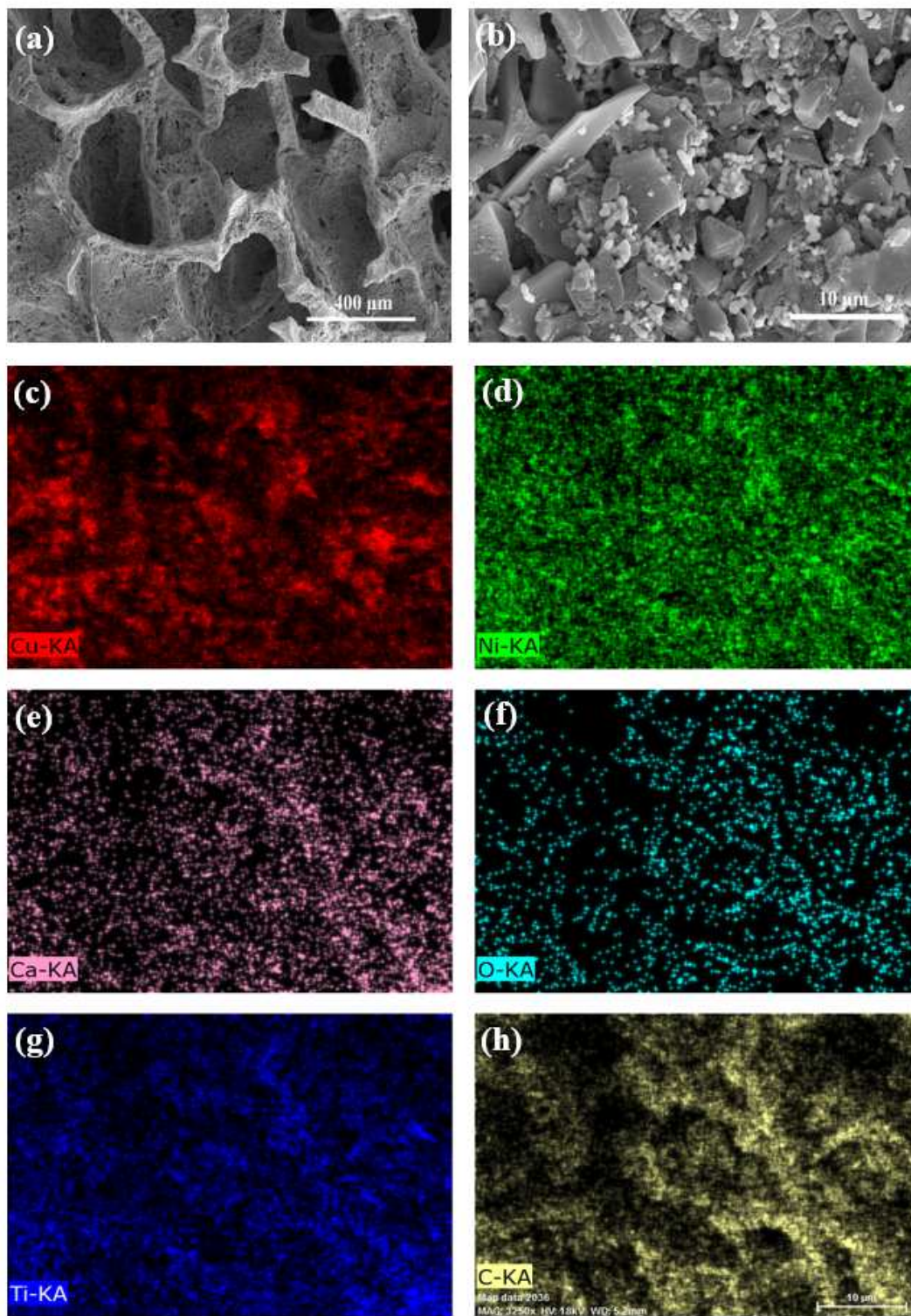


Figure 3

EDS mapping and distribution of the as-prepared $\text{CaCu}_3\text{Ti}_4\text{O}_{12}$ (CCTO) slurry on the electrode: (a) FESEM image of the CCTO coated Ni Foam, (b) The distribution of the CCTO catalyst on the electrode, (c) Cu element (Red), (d) Ni element (Green), (e) Ca element (Pink), (f) O element (Cyan), (g) Ti element (Blue), (h) Carbon element (Yellow).

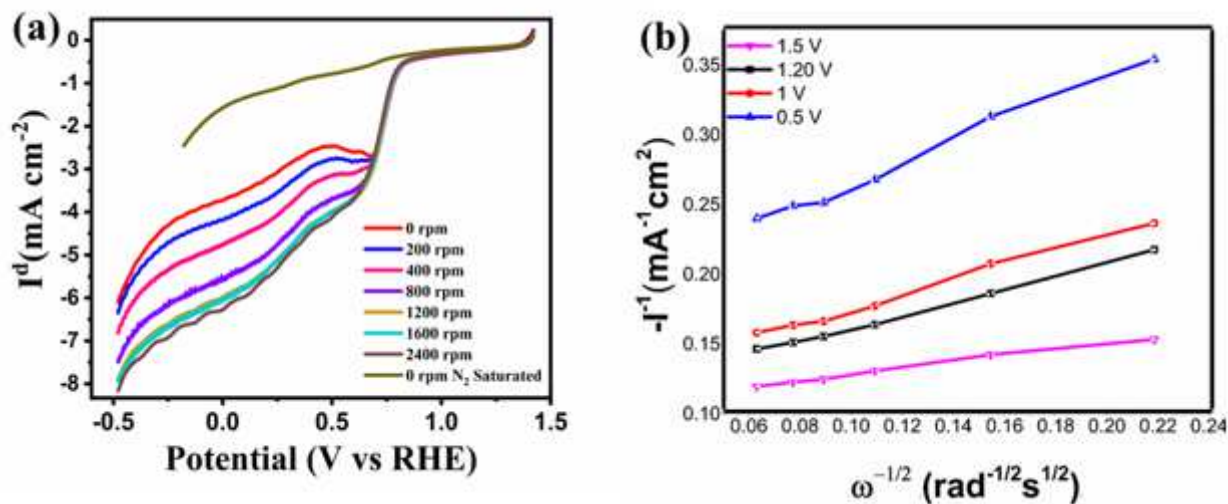


Figure 4

ORR electro-chemical analysis in 0.1 M KOH solution, O₂ purged (a) RDE graphs of CCTO at different rotations in the potential range of 1.5 to -0.5V; (b) Koutecky – Levich graph of the material at various potentials (V).

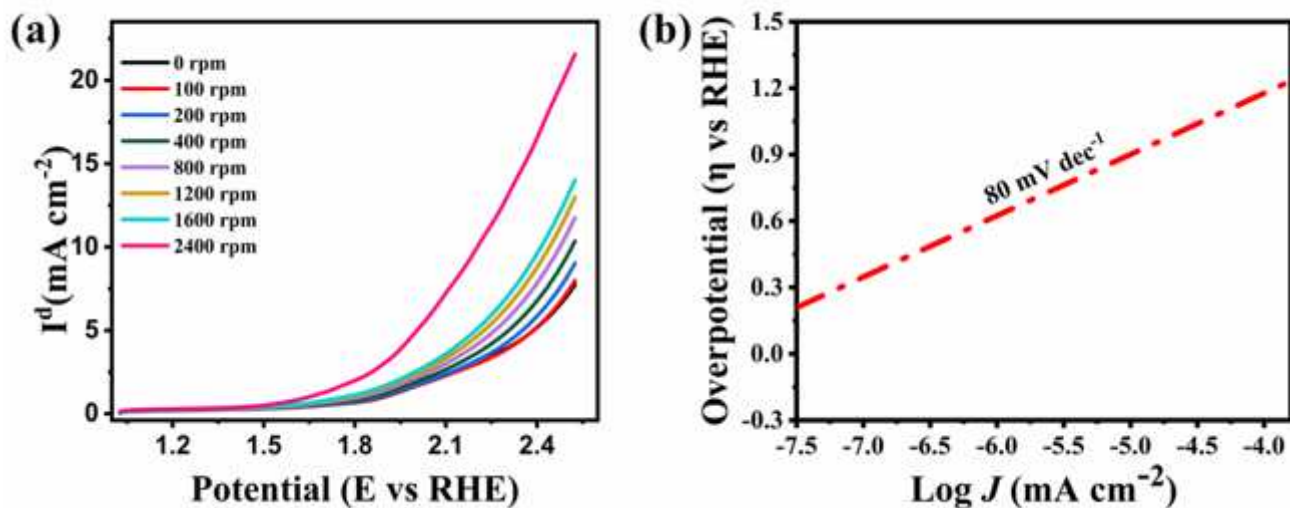


Figure 5

Electro-chemical investigation of OER in 1M KOH solution (N₂ saturated) (a) LSV graphs of CCTO at different rotations between the potentials of 0.0 – 2.4V

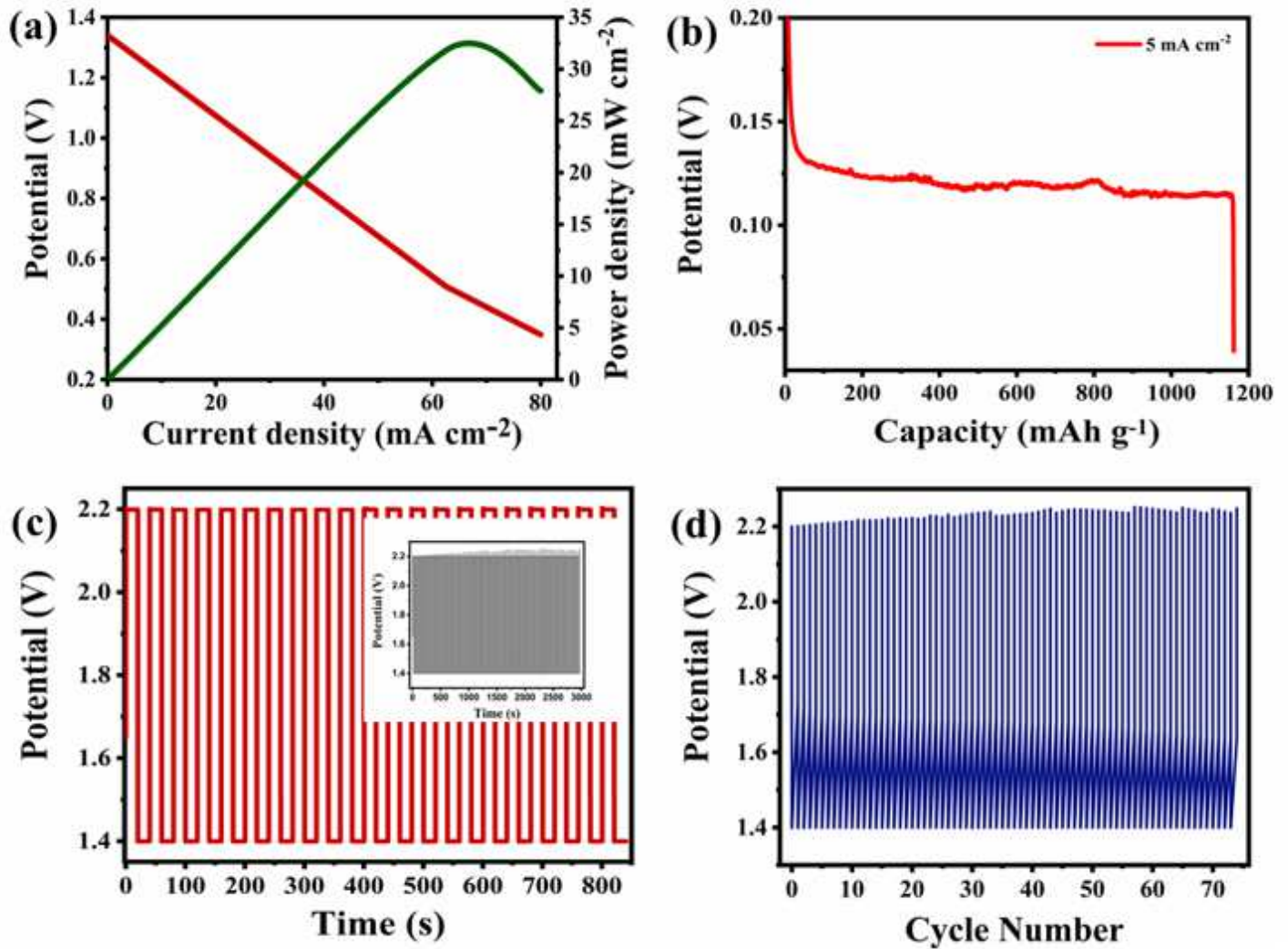


Figure 6

Performance of fabricated aqueous zinc-air battery. (a) Charge – Discharge curve with Power density of CCTO; (b) Discharge profile of CCTO at 5 mA cm^{-2} for continuous 30 hours. (c) Charge/discharge (Chronopotentiometric) curve for CCTO at 20 mA cm^{-2} with the potential range of 1.4-2.2 V for an hour (insight: displays charge/discharge polarization (Time vs. Potential) with extended cycles); (d) shows Voltage vs. Number of cycles.

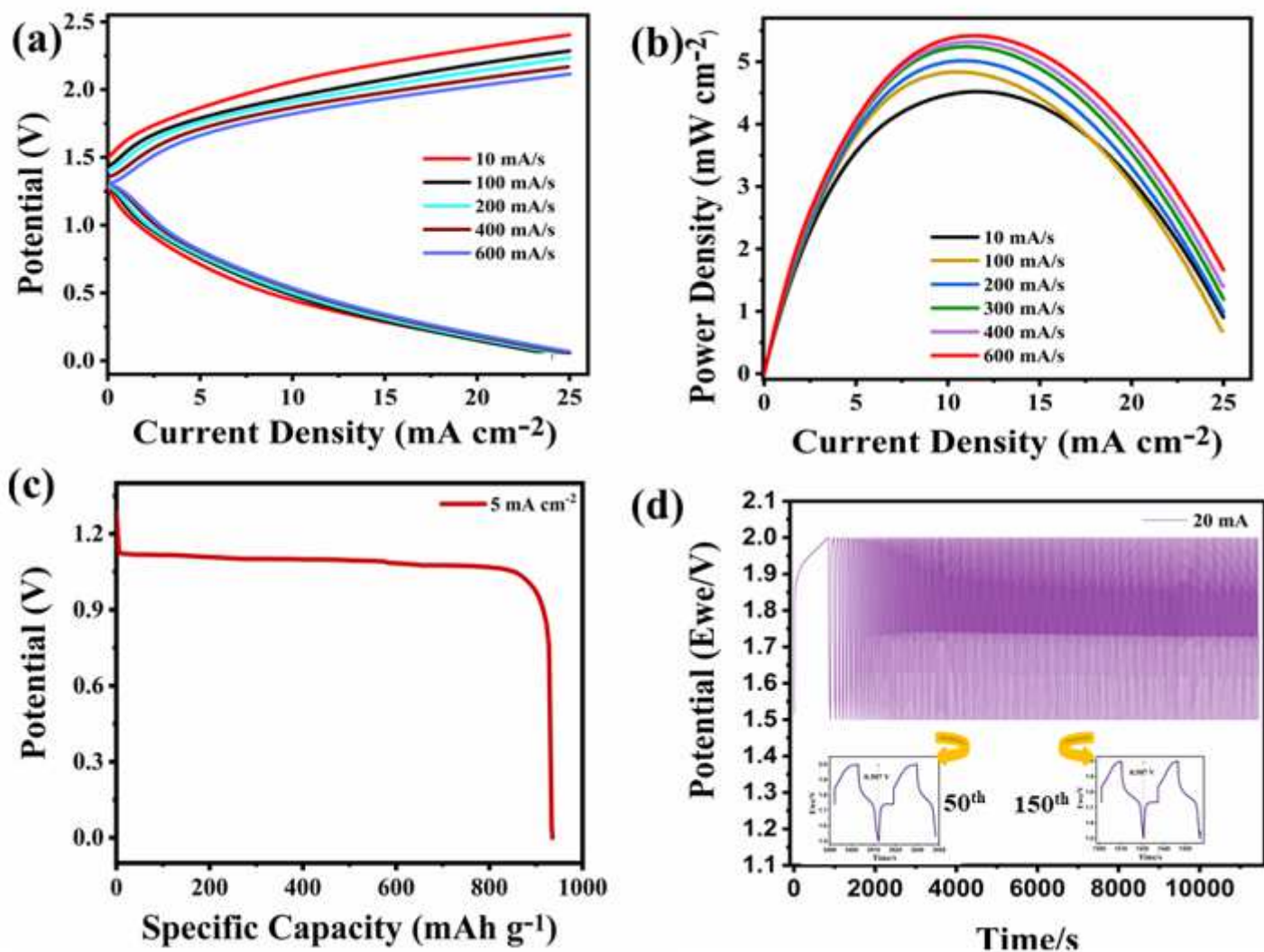


Figure 7

Performance of fabricated solid-state ZAB. (a) Charge/Discharge of the cell at various scan rates; (b) CCTO power density; (c) CCTO discharge profile (Capacity vs. Potential) at 5 mA cm^{-2} ; (d) Chronopotentiometric charge/discharge cycles for CCTO at 20 mA with the potential range of 1.5-2.0 V, (insight: shows charge/discharge potential cycles).

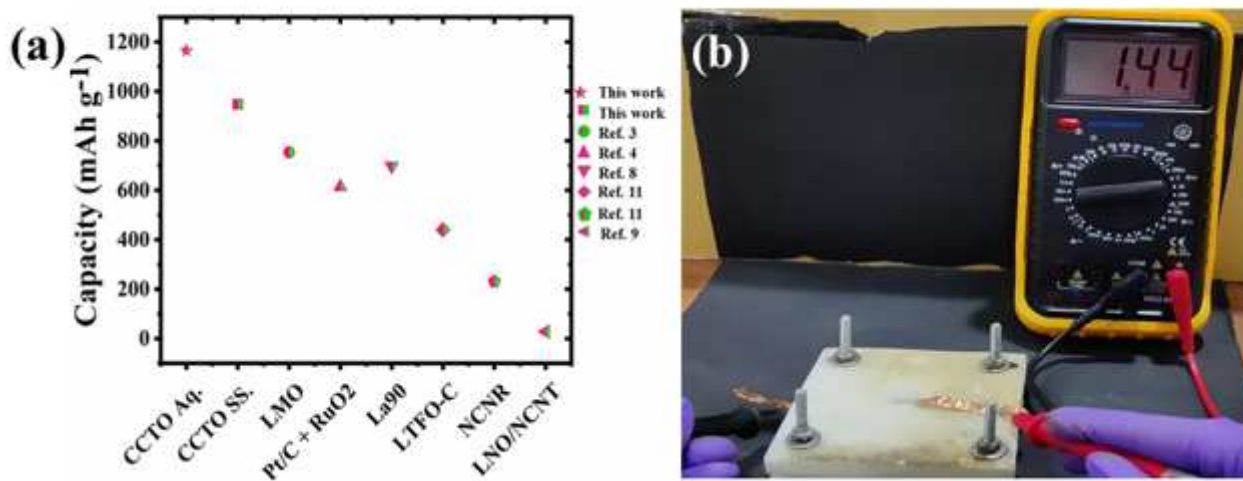


Figure 8

(a) Battery Potential vs. Cycle Number plot for filter paper battery; (b) Comparison of various zinc-air batteries with CCTO; (c) shows the potential of designed solid-state zinc-air cell giving the OCV of 1.44 V.

Supplementary Files

This is a list of supplementary files associated with this preprint. Click to download.

- [supplementaryfileCCTO.docx](#)